Pure Appl. Chem., Vol. 81, No. 9, pp. 1615–1634, 2009.
doi:10.1351/PAC-CON-08-11-11

Fluorescence of oligonucleotides adsorbed onto the thermoresponsive poly(isopropyl acrylamide) shell of polymer nanoparticles: Application to bioassays*

José M. G. Martinho‡, Telmo J. V. Prazeres, Leila Moura, and José P. S. Farinha

Centro de Química-Física Molecular and IN - Institute of Nanosciences and Nanotechnology, Instituto Superior Técnico, Av. Rovisco Pais, 1, 1040-001 Lisbon, Portugal

Abstract: The fluorescence of a rhodamine X dye covalently linked to the 5' terminus of a 25-mers thymine oligodeoxynucleotide (dT_{25}-ROX), adsorbed on the shell of thermoresponsive core-shell polymer particles, was used to probe the polarity, mobility, and distribution of the oligodeoxynucleotides (ODNs) in the shell. The particles have a glassy core of poly(methyl methacrylate) (PMMA) with a 67-nm radius, and a thermoresponsive shell of poly(*N*-isopropyl acrylamide) (PNIPAM) whose thickness changes from 42 nm at 11 °C to 5 nm at 45 °C. The variation in polarity of the shell with temperature was obtained both from the lifetimes and from the solvatochromic shifts of the dye and shows a sharp transition at the volume phase transition temperature (T_{VPT}) of the PNIPAM shell. Förster resonance energy transfer (FRET) between dT_{25}-ROX and a malachite green (MG)-labeled ODN (dT_{25}-MG) was used to obtain the distribution of the ODNs in the thermoresponsive shell. Our results show that at 23 °C (below T_{VPT}) the ODNs are distributed inside the shell, sensing an environment similar to water. At this temperature, the PNIPAM shell is composed of hydrated chains with high mobility, as probed by the fluorescence anisotropy of dT_{25}-ROX. By increasing the temperature above T_{VPT}, the shell collapses and the chain mobility drastically slows down owing to the anchoring of the ODN to the dense shell of PNIPAM. Furthermore, FRET shows that the ODNs are absorbed on the 5-nm-thick collapsed shell but extend into the water. The polarity probed by the ROX averages the dyes distributed in the interior of the particle shell and in water, with 60 % of the dyes outside the particle shell (i.e., sensing pure water). Another indication that above the T_{VPT} most of the ODNs are oriented with the dye toward the water phase is that the mobility of the dye covalently bound to the ODNs is identical in water and in the collapsed particle shell.

The hybridization efficiency between an ODN supported in the particle shell (by adsorbing the ODN below T_{VPT} and subsequently increasing the temperature above T_{VPT}) and the complementary ODN in solution is identical to that of hybridization in water. This result opens good perspectives toward the use of the core-shell thermoresponsive nanoparticles as supports in DNA bioassays.

Keywords: core-shell nanoparticles; DNA bioassays; energy transfer; fluorescence and fluorescence anisotropy; oligonucleotides; thermoresponsive nanoparticles.

---

*Paper based on a presentation at the XXII[nd] IUPAC Symposium on Photochemistry, 28 July–1 August 2008, Gothenburg, Sweden. Other presentations are published in this issue, pp. 1615–1705.
‡Corresponding author: Tel.: 351-218419250; E-mail: jgmartinho@ist.utl.pt

INTRODUCTION

Fluorescence is an excellent tool to probe the structure and dynamics of polymers and biological systems [1,2]. The success of fluorescence resides in the high sensitivity of the technique (the fluorescence of a single molecule can be detected under a confocal microscope) and the specificity of fluorescence parameters (spectrum, quantum yield, lifetime, and polarization) to the local environment [1]. An electronically excited fluorescent molecule can be involved in a series of intermolecular processes (energy transfer, electron transfer, excimer or exciplex formation, etc.) with other species, which can be used to determine nanometer-scale distances [3–6], obtain information on the structure and size of nanodomains (energy transfer) [7], and study the dynamics (excimer and exciplex formation) of polymer chains [8,9].

On the other hand, polymer nanoparticles with well-defined size in the sub-micrometer range are currently used as supports in a large number of biotechnological, pharmaceutical, and medical applications, including diagnostics, bioseparation, imaging, cosmetics, drug delivery systems, targeting, and microarrays [10]. For biological applications, particles with a hydrophilic shell and a glassy core (core-shell morphology) are very promising since fluorescent or magnetic particles can be prepared by changing the core, while the shell can be tailored to improve the adsorption of biomolecules (ODNs, proteins) or their covalent binding to functional bioreactive groups introduced during the particle synthesis [11,12]. Among the core-shell particles, those that react to an external stimulus like pH, electrical and magnetic field, ionic strength, and temperature are specially promising [13–15].

Core-shell nanoparticles have been prepared with a glassy polystyrene (PS) or poly(methyl methacrylate) (PMMA) core and a thermoresponsive poly(*N*-isopropyl acrylamide) (PNIPAM) shell. In water, PNIPAM exhibits a lower critical solution temperature (LCST) around the physiological temperature (31–35 °C). By increasing temperature above the LCST, the isolated chains undergo an entropic induced reversible phase transition from a solvated coil to a globular state. The transition depends on the subtle balance between the polymer ability to form hydrogen bonds with water through the amide groups and the hydrophobic interactions due to the hydrocarbon backbone and the side-chain alkyl groups. At temperatures below the LCST, a homogeneous solution of hydrated polymer chains in a random coil conformation exists, while above the LCST, the amide–water hydrogen bonds are disrupted, the bond and structured water are released, and the chain collapses into a globule owing to the interactions between the hydrophobic isopropyl groups. These thermoresponsive core-shell particles were shown to be very adequate to support oligodeoxynucleotides (ODNs) for applications in biological testing. To enhance the ability to adsorb the negatively charged ODN molecules, we prepared monodisperse core-shell particles with a glassy PMMA core and a cationic thermoresponsive shell of PNIPAM and aminoethyl methacrylate hydrochloride (AEMH), cross-linked with methylene bisacrylamide (MBA) [16].

The characterization of the nanoparticles is a prerequisite to optimize their use in several applications, namely, in bioassays where adsorbed or covalently linked ODNs on the hydrophilic shell of the nanoparticles can recognize the complementary target ODN in aqueous solution.

A polythymine ODN with 25 mers (dT_{25}) labeled at the 5'-terminus with a rhodamine X (dT_{25}-ROX) was adsorbed onto the PNIPAM shell. The spectral shifts of the fluorescence spectrum of ROX were used to probe the shell polarity [17], while the fluorescence anisotropy of the ROX probes the dynamics of the shell [18]. Substantial changes in polarity and mobility of the chains were observed around 32 °C, which coincides with the LCST of PNIPAM in water. Förster resonance energy transfer (FRET) between the dT_{25}-ROX (energy donor) and a 25 mers labeled with malachite green (MG) at the 5'-terminus (dT_{25}-MG) (energy acceptor) was used to calculate the distribution of the ODNs in the thermoresponsive PNIPAM shell (Fig. 1) [19].

These data allow us to design a bioassay using the thermoresponsive core-shell nanoparticles as supports for ODN sequences. Here we have chosen a sequence within the F5 gene, specifically containing the 1691G-A mutation, which is associated with the presence of the Lieden V factor. The pres-

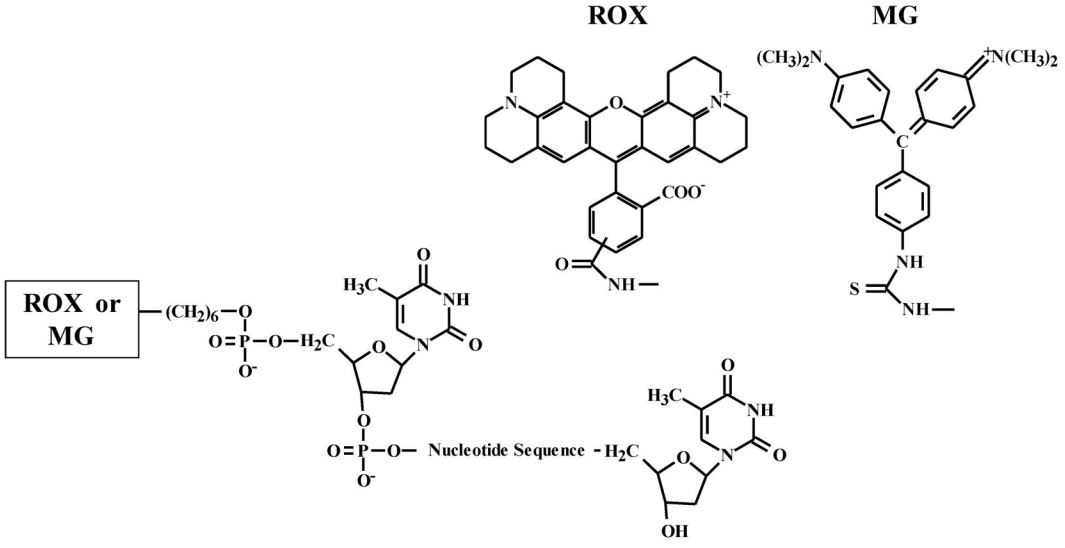

Fig. 1 Molecular structure of the ODNs labeled either with rodamine X (ROX in the image) or with malachite green (MG in the image).

ence of this factor leads to a five times greater risk of developing a blood clot (thrombosis). The hybridization was followed by FRET using ODN with the appropriate sequence (Gene-MG) and the complementary ODNs labeled with ROX (Cgene-ROX), labeled in opposite ends of the strands since the hybridization occurs in an antiparallel arrangement.

The results show that the efficiency of hybridization at 40 °C (pH 4.0, 0.18 M NaCl) is identical to the one observed when the Cgene-ROX is adsorbed onto the surface of polymer particles in a dispersion (0.015 wt %, pH 4.0, 0.18 M NaCl). The high efficiency obtained with the supported ODNs at 40 °C (above the volume phase transition, VPT) is due to the fact that the ODNs are fixed in the thin shell but oriented toward the solution. These results correlate very well with both the polarity and the FRET measurements that allow the calculation of a shell diameter larger than the one calculated by dynamic light-scattering (DLS).

EXPERIMENTAL

Materials

The ROX- and MG-labeled ODNs were purchased from Thermo (Germany) in the lyophilized form (HPLC grade).

Core-shell nanoparticles

The polymer core-shell particles were obtained by a two-stage emulsion polymerization technique in water, using methyl methacrylate (MMA, from Aldrich, 99 %), *N*-isopropyl acrylamide (NIPAM, from Acros, 99 %), and AEMH (from Acros, 99 %) monomers. 2,2'-Azobis(2-amidinopropane) dihydrochloride (V50, from Wako Chemicals) was used as initiator, and dodecyl ethyl dimethyl ammonium bromide (DEDAB, from Fluka AG, >98 %) was used as surfactant. A small amount of MBA (from Kodak, electrophoretic grade) was used to cross-link the polymer chains. In the first stage, the PMMA core was prepared using a mixture of DEDAB (0.06 g/100 g of mixture, ~2 mM) at a concentration below its critical micelle concentration (CMC ≈ 13–14 mM) [20], V50 (0.05 g), and MMA (5 g) under

N_2(g) atmosphere at a constant temperature of 70 °C, until ca. 80 % conversion was reached. In the second stage, a mixture of NIPAM/MBA/AEMH (0.88 g/0.10 g/0.031 g) was added in several shots to the reaction medium at 70 °C for at least 2 h. The global conversion was 100 %, and the solid content of the final particle dispersions was ca. 9.5 wt %.

Sample preparation

The ODNs were dissolved in a phosphate buffer solution (10 mM phosphate, 10 mM NaCl, pH 5.5 or 1 mM phosphate, 1 mM NaCl, pH 4.0) prepared using sodium dihydrogenophosphate 1-hydrate ($NaH_2PO_4 \cdot H_2O$, Panreac), hydrochloric acid (HCl, 1 N, Panreac), 1 mM of sodium chloride (NaCl, Merck), and Milli-Q water. Before the measurements, the samples containing nanoparticles and ODNs were incubated at room temperature (23 °C) for at least 3 h in order to guarantee the adsorption equilibrium. For DLS and fluorescence measurements, we used less than 0.0150 wt % of nanoparticles to avoid multiple scattering and contamination of the fluorescence by the scattered light. The maximum concentration of the ODN was adjusted in order to satisfy the condition that more than 95 % of the ODNs are adsorbed. This level of adsorption was confirmed by fluorescence measurements of the supernatant obtained by centrifugation of an equilibrated dispersion at 14 000 rpm for 20 min. For FRET measurements, the concentration of nanoparticles was kept constant at 0.0150 wt %, with the donor (dT_{25}-ROX) concentration at 3.6 nmol/l, whereas the concentration of acceptor (dT_{25}-MG) was changed from 5.4 to 45.3 nmol/l.

For hybridization experiments, an ODN labeled at the 5' end with MG (Gene-MG: 5' G AGA GAC ATC ACC TCT GGG CTA ATA 3') and the complementary with ROX in the 3' end (Cgene-ROX: 5' TAT TAG CCC AGA GGT GAT GTC TCT C 3') were used. The dispersion of the nanoparticles (0.0150 wt %) at pH = 4.0 with the Cgene-ROX at concentrations that assure a percentage of ODNs adsorbed onto the particles higher than 95 %, were maintained at room temperature during the night under stirring. The temperature was raised to 40 °C and kept under stirring for more 2–3 h before recording the fluorescence spectrum. The solutions containing the Cgene-ROX (25 nM) and Gene-MG (35 nM) were then prepared and maintained for 2–3 h at 40 °C under stirring before the fluorescence measurements. The ionic strength of the solutions was adjusted by adding NaCl to a concentration of 0.18 M to optimize the hybridization.

Fluorescence spectra and decay curves

The absorption spectra were measured in a Shimadzu UV-3101PC spectrometer and the fluorescence spectra in a SLM-AMINCO 8100 Series2 spectrofluorimeter, in both cases using 5 × 5 mm quartz cuvettes. For the steady-state anisotropy measurements, the sample is excited with vertically polarized light and the fluorescence-polarized components parallel ($I_{||}$) and perpendicular ($I_{\perp}$) to the direction of the excitation light were acquired using Glan–Thompson polarizers. The fluorescence spectra were corrected for the response of the detection system. Temperature was kept at 23 °C by a water-circulating bath (±0.5 °C, Julabo F25). Time-resolved fluorescence decays with picosecond resolution were obtained by the single-photon timing technique using laser excitation at 575 nm. The system consists of a modelocked Coherent Inova 440-10 Ar ion laser synchronously pumping a cavity-dumped Coherent 701-2 dye laser using rhodamine 6G, which delivers 5–6 ps pulses at a repetition rate of 800 kHz. The fluorescence emission was observed at 615 nm using a cutoff filter to effectively eliminate the scattered light from the sample. The fluorescence was selected by a Jobin-Yvon HR320 monochromator with a grating of 100 lines/mm and detected by a Hamamatsu 2809U-01 microchannel plate photomultiplier. The polarized fluorescence intensities were recorded by exciting the sample with vertical polarized light, being the fluorescence-polarized components recorded using a Glan–Thompson polarizer. The experimental decay curves were fitted to simulated curves [21] using a nonlinear least-squares reconvolution method based on the Marquard algorithm [22].

Dynamic light-scattering

The hydrodynamic particle radii were obtained by DLS (Brookhaven Instruments: BI-200SM goniometer and BI-9000AT autocorrelator) using a He-Ne laser (Spectra Physics, model 127 with 35 mW at 632.8 nm) and an avalanche photodiode detector. Diluted particle dispersions (0.005 wt % of nanoparticles in 1 mM phosphate buffer solution, 1 mM NaCl, pH = 4.0) were measured at 90° under controlled temperature (±0.1 °C). The autocorrelation functions were analyzed by Laplace inversion (CONTIN) from Brookhaven package software.

RESULTS

Dynamic light-scattering

The hydrodynamic radius of the glassy PMMA core, R_c = 67 nm, was measured by DLS of model PMMA nanoparticles synthesized in similar conditions as those used to prepare the core of the core-shell particles [16] and does not change in the interval of temperatures used. On the other hand, the core-shell particles change their diameter in response to changes in temperature, while maintaining a narrow size distribution (with standard deviation below 0.01 over the full temperature range). The hydrodynamic radius of the core-shell particles show a large and broad VPT, centered at a temperature $T_{VPT} \approx 30$ °C (Fig. 2), close to the LCST of PNIPAM in water [23–26].

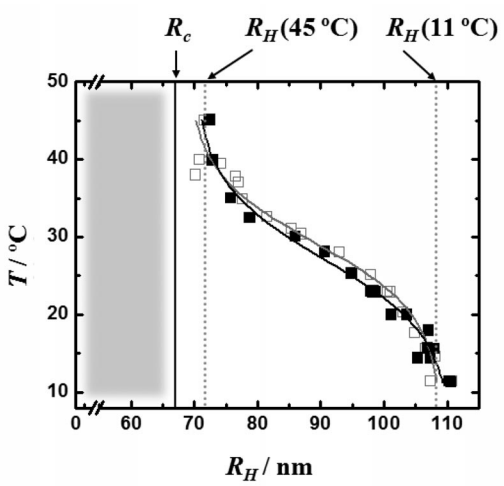

Fig. 2 Hydrodynamic radii of the core (R_c) and of the particles (R_H), determined by DLS of dispersions (5.0×10^{-3} wt %) in aqueous phosphate buffer solution (1 mM, and 1 mM NaCl, pH = 4.0) at different temperatures: (□) without ODNs adsorbed and (■) with the maximum adsorption of ODNs used for FRET measurements. The black and gray solid lines correspond to fitting curves to the experimental data.

The size of the particles, determined by DLS between 11 and 45 °C, shows a broad transition ~30 °C due to the VPT of the thermoresponsive PNIPAM shell of the particles. The radius of the particle changes from 109 nm at 11 °C to 72 nm at 45 °C, due to the collapse of the PNIPAM shell in the glassy PMMA core (R_c = 67 nm) of the particles, which implies a variation of the shell width from 42 nm (11 °C) to 5 nm (45 °C).

The shell of the particles is positively charged at low pH, with the charges coming from the amidine groups of the initiator (V-50) and the amino groups of the AEMH comonomer.

At about 11 °C (far below the T_{VPT}), the particles have the highest hydrodynamic radius ($R_H \approx$ 109 nm) because the PNIPAM chains of the particle shell adopt extended conformations due to hydrogen bonding with the water molecules. Because the hydrodynamic radius of the core is R_c = 67 nm, the length of the PNIPAM shell can be estimated as $L_{shell} = R_H - R_c$ = 42 nm. At 45 °C (ca. 15 °C above the temperature of the VPT), the hydrodynamic radius of the particles is reduced to $R_H \approx$ 72 nm as a result of the collapse of the PNIPAM chains onto the PMMA core, induced by the dehydration of the shell and the release of the bound and structured water. Even though the PNIPAM shell is reduced to a thickness of only L_{shell} = 5 nm, corresponding to ca. 7 % of its low-temperature volume, previous results indicate that dT_{25}-ROX molecules adsorbed to the shell sense a quite hydrophilic environment, with an equivalent polarity equal to a mixture of 30 % (v/v) of water in dioxane [17,27].

In Fig. 2, it is also apparent that the behavior of the particles depends only slightly on the amount of adsorbed ODNs. This indicates that this amount of adsorbed ODN is not enough to change the net charge of the particles. In fact, the total particle charge should be equal to the charges expected from the comonomer (ca. 30 μmol/g) plus the charges resulting from the initiator (estimated as ca. 60 μmol/g). Therefore, for a total charge close to 100 μmol/g, the effective neutralization achieved by the adsorption of ODNs is relatively small.

Fluorescence measurements

Figure 3 shows the excitation and fluorescence spectra of the dT_{25}-ROX (10^{-8} M) in a 10 mM phosphate buffer solution (pH 5.5) and 10 mM NaCl ionic strength at 22 °C. Rhodamine X is a derivative of rhodamine 101, which is known to have a fluorescence quantum yield close to 1.0, irrespective of temperature [28].

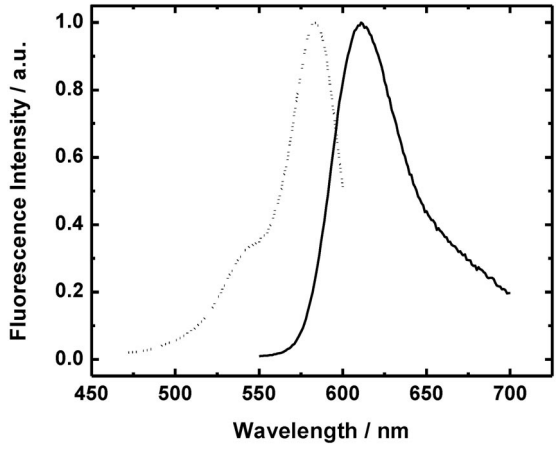

Fig. 3 Normalized excitation (·····) and emission (—) fluorescence spectra of the dT_{25}-ROX (10^{-8} M in 10 mM phosphate buffer, pH 5.5, and 10 mM NaCl) at 22 °C. The fluorescence emission and excitation spectrum were recorded at λ_{exc} = 535 nm and λ_{em} = 635 nm, respectively.

Rhodamine X, like other rhodamines (rhodamine B, rhodamine 101, etc.), has a carboxylphenyl group in their structure and may participate in an equilibrium between the lactone, cationic, and zwitterionic molecular forms [29]. Both the zwitterion and the cation strongly absorb in the visible region due to the π-electronic system of the xanthene moiety. The lactone has the π-electronic system inter-

rupted, and its absorption occurs in the UV spectral region [29]. The zwitterion is stabilized by hydrogen bonding and the polarity of the solvent, being the main species in polar protic solvents at neutral pH. Therefore, the fluorescence of dT_{25}-ROX in the phosphate buffer solution (pH 5.5) is simply due to the zwitterions, the unique species absorbing in the visible region. Aggregation of the dye was not detected as expected due to its low concentration and the presence of electrostatic repulsive forces between the phosphate groups of the ODN. The fluorescence spectra in phosphate buffer are practically invariant with temperature in the range between 15 and 45 °C. The fluorescence quantum yield of dT_{25}-ROX was determined using as reference rhodamine 101 in ethanol ($\Phi = 1.0 \pm 0.2$) [28]. The quantum yield in water and in the buffer solution is equal to 0.90 ± 0.05, in the interval of 15–45 °C. The quantum yield is slightly lower than 1.0, probably due to water quenching by dissipation of electronic energy through a hydrogen bond (the deactivation involving the rotation of the amino groups is hindered in ROX).

The decays of dT_{25}-ROX in the buffer solution and after adsorption on the polymer nanoparticles are well fitted by a single exponential function at all temperatures [17]. Figure 4 shows the lifetimes of dT_{25}-ROX in solution and when adsorbed in the polymer nanoparticles at pH = 5.5, as a function of temperature.

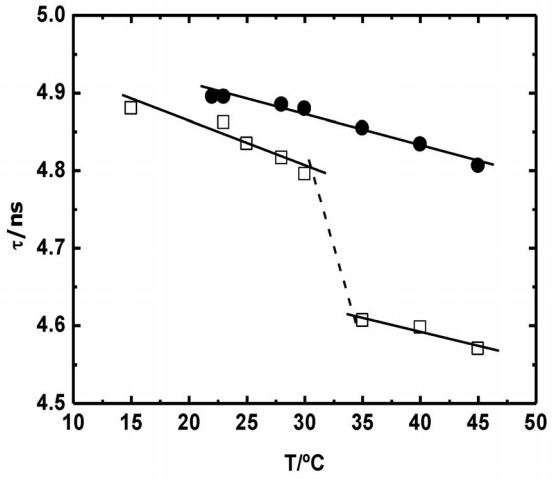

Fig. 4 Temperature dependence of dT_{25}-ROX fluorescence lifetimes in (●) buffer solution (10^{-8} M, pH = 5.5) and (□) adsorbed on the core-shell polymer particles (10^{-8} M, pH = 5.5, 0.0125 wt % of polymer particles).

In solution, the lifetime decreases slightly and continuously with temperature increase, while for the dT_{25}-ROX adsorbed onto the particles, a clear break was observed around the T_{VPT} of the PNIPAM shell. A similar behavior was shown for the variation of the size of the nanoparticles with temperature (cf. Fig. 2). In solution, the slight decrease in the dT_{25}-ROX lifetime with temperature is attributed to the increase of quenching by water [30], in accordance with a quantum yield in water slightly lower than 1.0, observed in acidic ethanol.

The abrupt changes observed in the lifetime of the adsorbed dT_{25}-ROX by increasing the temperature cannot be due to water quenching, which should decrease with the dehydration of the shell. As the quantum yield of dT_{25}-ROX is close to 1, the main deactivation process is the emission of light, with rate constant, k_f. The radiative rate constant for fluorophores with a mirror symmetry between the absorption and the fluorescence spectra with respect to the frequency of the $0 \leftrightarrow 0$ transition, is well described by the Strickler–Berg equation [31],

$$k_f = n^2 \times \frac{(2.880 \times 10^{-9})}{<\bar{\nu}^{-3}>} \int \frac{\varepsilon(\bar{\nu})}{\bar{\nu}} d\bar{\nu} = k_{f0} \times n^2 \quad (1)$$

where n is the refractive index of the medium, $\varepsilon(\bar{\nu})$ is the molar absorption coefficient at wavenumber $\bar{\nu}$, and ,$<\bar{\nu}^{-3}>$ is averaged over the fluorescence spectrum.

In this case, the variation of the lifetime ($1/\tau = k_f + k_{nr} \sim k_f$) can be interpreted by the variation of the refractive index of the PNIPAM shell during the VPT. This is so, because the nonradiative rate constant, k_{nr}, is relatively small and should not change significantly with temperature. Since the absorption spectrum of dT_{25}-ROX changes only slightly in the temperature interval 15–45 °C, k_{f0} can be considered constant with temperature. Using the value of $k_{f0} = 0.112$ ns^{-1} calculated for water/dioxane mixtures [17], it is possible to calculate the refractive index from the lifetimes using eq. 1. The square of the refractive index should be a weighted average, given by

$$n^2 = f_{H_2O} n^2_{H_2O} + (1 - f_{H_2O}) n^2_{Shell} \quad (2)$$

where f_{H_2O} is the fraction of ROX surrounded by water, n_{H_2O} [32] is the refractive index of water, and n_{shell} is the refractive index of the particle shell. At 45 °C, the refractive index of the shell is very similar to that of PNIPAM ($n_{PNIPAM} = 1.48$) [33], because the shell is completely collapsed onto the particle core. By this method, we estimate that the fraction of ODNs with the dye oriented toward the water is $f_{H_2O} = 60$ %, with the remaining ODN having the ROX-labeled chain end oriented toward the PMMA core. Figure 5 shows the solvatochromic shifts measured for dT_{25}-ROX in the aqueous buffer solution and when adsorbed on the shell of the particles. The solvatochromic shifts of the adsorbed dT_{25}-ROX relative to water ($\Delta\bar{\nu} = \bar{\nu} - \bar{\nu}_{H_2O}$) are almost zero below the T_{VPT}, but increase continuously above this temperature, reaching $\Delta\bar{\nu} \sim 240$ cm^{-1} at 40 °C, and remaining almost constant for higher temperatures. From the plot, we can see that the dT_{25}-ROX adsorbed in the shell senses the polarity of bulk water for temperatures below 20 °C, but above this temperature the spectrum shifts to the blue because the local polarity probed by ROX decreases.

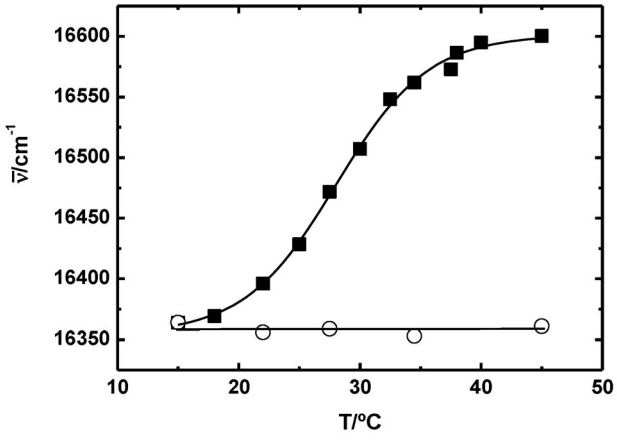

Fig. 5 Temperature dependence of the wavenumber ($\bar{\nu}$) of the fluorescence emission maximum of dT_{25}-ROX in: (○) buffer solution (10^{-8} M, pH = 5.5) and (■) adsorbed onto the core-shell of polymer particles (10^{-8} M, pH = 5.5, 0.0125 wt % of nanoparticles).

Fluorescence anisotropy

Fluorescence polarization is a powerful tool to probe the dynamics of fluorophores in both homogeneous and heterogeneous media [1]. When a population of fluorophores is irradiated by linearly polarized light, those whose transition dipole moments are oriented in a direction close to the electric vector of the incident beam are preferentially excited (photoselection). The emission of light from this population is anisotropic, and any molecular motion that changes the direction of the transition dipole moment leads to a decrease in the absolute value of the anisotropy and consequently to the depolarization of the fluorescence. One of the main mechanisms of fluorescence depolarization is the rotation of the probe during its lifetime. For free-rotational Brownian motion, the anisotropy decays to zero, but when the rotation is hindered a nonzero constant value is obtained at long times. This is caused by the fact that during the fluorescence decay, a random distribution of orientations is achieved for the free rotation but not when the rotational motion is hindered [1,2].

The fluorescence anisotropy of a fluorophore electronically excited by a δ-pulse of light is given by

$$r(t) = \frac{I_{||}(t) - I_{\perp}(t)}{I_{||}(t) + 2I_{\perp}(t)} = \frac{I_{||}(t) - I_{\perp}(t)}{I(t)} \tag{3}$$

where $I(t)$ is the fluorescence decay recorded at the magic angle (54.7° to the direction of the vertical polarized excitation light) and $I_{||}(t)$ and $I_{\perp}(t)$ are the parallel and perpendicular polarized fluorescence decays to the direction of polarization of the excited light, respectively. The steady-state anisotropy is related to the time-resolved anisotropy by

$$r_{ss} = \frac{\int_0^{\infty} I(t) r(t)\, dt}{\int_0^{\infty} I(t)\, dt} \tag{4}$$

and can be calculated from the polarized steady-state fluorescence intensities

$$r_{ss} = \frac{I_{||} - GI_{\perp}}{I_{||} + 2GI_{\perp}} \tag{5}$$

where G is an instrumental correction factor, which takes into account the sensitivity of the monochromator to the polarization of the light. In the case of the polarized decays, $G = 1$, because the light passes through a depolarizer mounted at the entrance slit of the monochromator before being detected.

Figure 6 shows the steady-state anisotropy (r_{ss}) of dT_{25}-ROX in phosphate buffer solution and when adsorbed on the shell of the polymer particles at several temperatures.

In solution, r_{ss} decreases from 0.10 ± 0.02 at 15 °C to 0.04 ± 0.02 at 50 °C. The decrease of anisotropy with temperature is mostly due to the increase of the rotational diffusion coefficient of dT_{25}-ROX with temperature. The anisotropy of dT_{25}-ROX was measured in very dilute nanoparticle dispersions (0.0125 wt %), to avoid the contamination of the fluorescence by the scattered light. The experimental conditions were adjusted in order to ensure that more than 95 % of the ODNs were adsorbed. Thus, the anisotropy reports solely the dynamics of the ODNs adsorbed on the thermoresponsive shell.

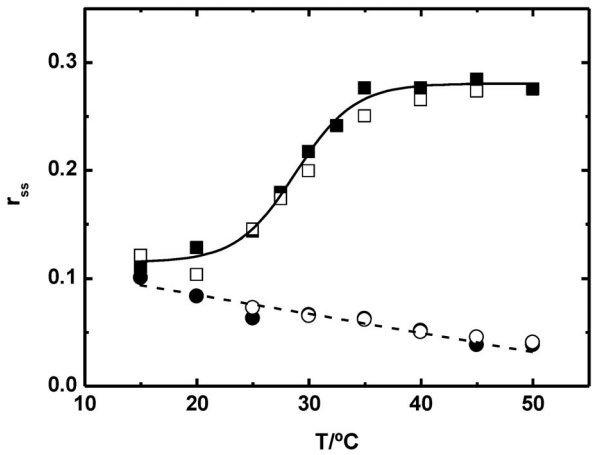

Fig. 6 Plot of the steady-state anisotropy (r_{ss}) of dT_{25}-ROX as function of temperature in (●, ○) 10 mM phosphate buffer solution and ionic strength of 10 mM NaCl (10^{-8} M, pH = 5.5) and (■, □) adsorbed on the core-shell nanoparticles (10^{-8} M, pH = 5.5, 0.0125 wt % of nanoparticles). The closed symbols refer to experimental r_{ss}, while the open symbols refer to r_{ss} calculated from the polarization decays using eq. 4.

The steady-state anisotropy, r_{ss}, of dT_{25}-ROX in solution and when adsorbed to the particles show a very different behavior. The r_{ss} values of the adsorbed dT_{25}-ROX are always higher than those in solution and increase with temperature, reaching a plateau (0.28 ± 0.02) for temperatures higher than 35 °C. At lower temperatures, the PNIPAM shell is well solvated by the water molecules; consequently, the shell is more mobile and the water content is higher than at high temperature. The adsorbed dT_{25}-ROX has enough freedom to move; behaving similarly to the ODN in solution (the r_{ss} values for dT_{25}-ROX in solution and adsorbed are very close at 15 °C). As the temperature is increased above the T_{VPT}, the shell dehydrates, its volume decreases, and the dynamics of the PNIPAM chains slow down. The ODNs become entrapped in this collapsed polymeric network, resulting in a drastic decrease in mobility with the consequent increase of the steady-state anisotropy until attaining a plateau at temperatures above T_{VPT}.

Figure 7 shows the anisotropy of dT_{25}-ROX (10^{-8} M) at 23 °C in 10 mM phosphate buffer (pH 5.5 and 10 mM NaCl). The anisotropy is well fitted with a sum of two exponentials,

$$r(t) = \beta_1 \exp(-t / \theta_{slow}) + \beta_2 \exp(-t / \theta_{fast}) \quad (6)$$

with correlation times describing slow (θ_{slow}) and fast (θ_{fast}) dynamics and the sum of the pre-exponential factors being equal to the fundamental anisotropy, $r_0 = \beta_1 + \beta_2$. A similar behavior for ODNs labeled with carboxytetramethylrhodamine (TAMRA) has been observed elsewhere [34]. The slow correlation time is attributed to the rotational motion of the ODN as a whole, while the fast correlation time is attributed to the local motion of the ROX covalently bound by the hexyl tether to the ODN, that can be described by a wobbling in a cone motion [35–37]. The experimental value $r_0 = 0.37 \pm 0.01$ obtained for dT_{25}-ROX in solution is in good agreement with the reported value of $r_0 = 0.373 \pm 0.002$ for xanthene derivatives [34]. The value is very close to the theoretical value of $r_0 = 0.4$ for $S_1 \leftarrow S_0$ absorption and collinear transition dipole moments for absorption and emission [1]. Recently, it was shown that rhodamine 101 is good anisotropy standard with limiting anisotropy precisely equal to the theoretical value of $r_0 = 0.4$ by electronic excitation in S_1 [38].

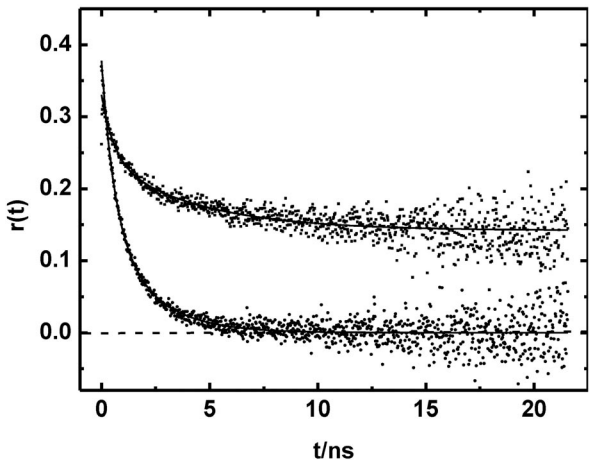

Fig. 7 Fluorescence anisotropy decay of 10^{-8} M dT_{25}-ROX: on (*bottom curve*) 10 mM phosphate buffer, pH 5.5, and 10 mM NaCl at 23 °C; and (*top curve*) adsorbed on the shell of the nanoparticles (pH 5.5, 0.0125 wt % of particles) at 30 °C The solid lines are the fitting curves using eq. 6 and 7, respectively.

The fluorescence anisotropy of dT_{25}-ROX when adsorbed onto the thermoresponsive shell of the nanoparticles is shown in Fig. 8 for dT_{25}-ROX (10^{-8} M) adsorbed on 0.0125 wt % of particles at pH = 5.5 and 30 °C. The anisotropy does not decay to zero and can only be fitted with a sum of two exponentials plus a constant, according to

$$r(t) = \beta_1 \exp(-t / \theta_{\text{slow}}) + \beta_2 \exp(-t / \theta_{\text{fast}}) + r_\infty \tag{7}$$

This anisotropy behavior can be interpreted in terms of an "heterogeneous population model" that considers two populations of adsorbed ODNs: the *mobile* ODNs with a rotational diffusion similar to those in water, and the *immobilized* ODNs which do not have an overall rotation, but rather a local movement of ROX described by a wobbling-in-cone model [35–37]. Assuming this model the anisotropy is given by [18]

$$r(t) = r_0(1-S^2) \times e^{-t/\theta_\omega} + (1-\alpha) r_0 S^2 \times e^{-t/\theta_{olig}} + \alpha\, r_0 S^2 \tag{8}$$

where α is the fraction of *immobile* ODNs, S is the order parameter which gives an indication of the orientational distribution of the dye in the wobbling cone, θ_w is the correlation time of the wobbling motion, and θ_{oligo} is the correlation time of the ODN as a whole. The correlations times θ_w, θ_{oligo} can be obtained from the experimental correlation times. In the present case, it is possible to show that $\theta_w \sim \theta_{\text{fast}}$ and $\theta_{\text{oligo}} \sim \theta_{\text{slow}}$ [18].

Figure 8 shows that the fraction of ODNs immobilized in the particle shell increases with temperature with a drastic variation around T_{VPT}. Indicating that the ODNs become immobilized in the collapsed particle shell.

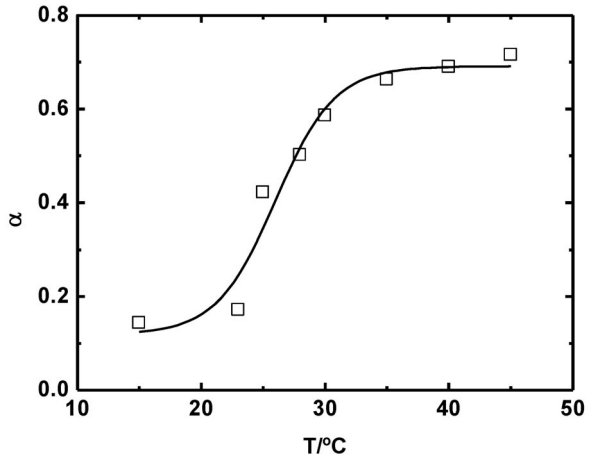

Fig. 8 Temperature dependence of the fraction of *immobile* ODNs for dT_{25}-ROX (M) adsorbed on the shell of the polymer particles (pH 5.5, 0.0125 wt % of particles).

The rotation correlation times of the "wobbling" motion of ROX attached to the ODN (θ_w) and of the whole ODN (θ_{oligo}) are plotted in Fig. 9. The motion of the ODNs as a whole is substantially hindered by temperature increase with a drastic variation around T_{VPT}, while the wobbling of ROX is practically unaffected by the transition. This result shows that dT_{25}-ROX adsorbed on the PNIPAM shell suffers an accentuated decrease in mobility, which reflects the collapse of the PNIPAM chains above T_{VPT}.

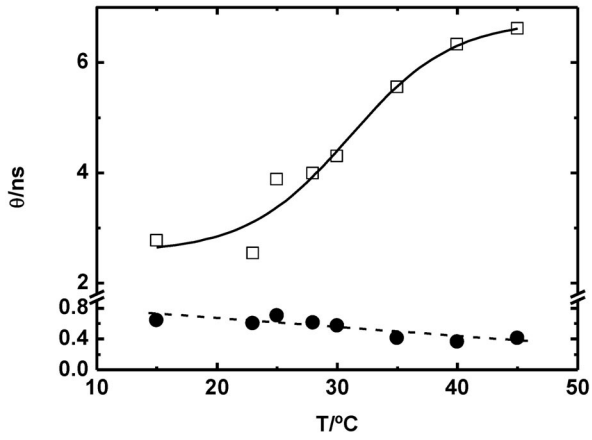

Fig. 9 Temperature dependence of the rotational correlation times for the "wobbling" motion of ROX attached to the ODN strand θ_w (●) and for the rotational diffusion of the whole ODN θ_{oligo} (□) for dT_{25}-ROX (10^{-8} M) adsorbed onto the polymer nanoparticles (pH = 5.5, 0.0125 wt % of particles).

Resonance energy transfer

The fluorescence spectra and decays of dT_{25}-ROX allow us to obtain some insight about the polarity of the PNIPAM shell, while the fluorescence anisotropy provides information on the mobility of the PNIPAM chains. This information is highly relevant for the optimization of these particles as supports for biomolecules. However, the distribution of the ODNs when physically adsorbed in the PNIPAM

shell of the nanoparticles is of utmost importance for such applications. We used FRET measurements to obtain this distribution. First, we model donor survival probability curves for different acceptor concentrations and simulated interface profiles, using a model that accounts for the kinetics of FRET between molecules in systems with restricted geometry. We generate a library of different donor and acceptor concentration profile curves and associated donor decay curves for each acceptor concentration used, and systematically compare the simulated curves with the experimental fluorescence donor decay curves.

The labeled ODN dT_{25}-ROX was chosen as the energy donor because it has a high fluorescence quantum yield and its fluorescence decay is single exponential in several media at different temperatures. For energy acceptor we have chosen a 25 mers polythymine ODN, labeled at the 5'-terminus with MG (dT_{25}-MG). MG was chosen because it is nonfluorescent in water at low pH, and the overlap integral between the fluorescence of ROX and the absorption spectrum of MG is very high (Fig. 10), yielding a Förster critical radius of R_0 = 6.8 nm (see below).

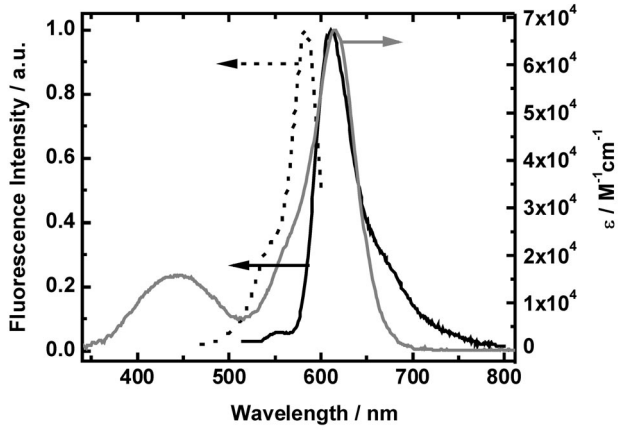

Fig. 10 Normalized excitation (···) and emission (—) fluorescence spectra of 9.8×10^{-7} M dT_{25}-ROX at λ_{em} = 615 nm and λ_{exc} = 510 nm, respectively, and absorption spectrum of 1.3×10^{-5} M dT_{25}-MG (—), at 23 °C.

The rate of FRET between an electronically excited donor molecule and an acceptor molecule separated by distance r is [39,40].

$$w(r) = \frac{3R_0^6\kappa^2}{2\tau_D}\frac{1}{r^6} \tag{9}$$

where τ_D is the unquenched donor lifetime, κ^2 is a dimensionless parameter associated with the relative orientation of the donor and acceptor transition dipole moments (dynamic averaging for a random distribution of dipoles yields $<\kappa^2>$ = 2/3), and the Förster radius R_0 is the characteristic distance at which the rate of energy transfer is equal to the rate of intramolecular deactivation. The value of R_0 (Å) can be calculated from

$$R_0 = 0.2108\left(\frac{\kappa^2\Phi_D}{n^4}J(\lambda)\right)^{1/6} \tag{10}$$

where Φ_D is the quantum yield of the donor fluorescence in the absence of the acceptor, and n is the refractive index of the medium. The spectral overlap integral $J(\lambda)$ (in M^{-1} cm^{-1} nm^4) was determined as

$$J(\lambda) = \int_0^{\infty} F_D(\lambda)\varepsilon_A(\lambda)\lambda^4 d\lambda \tag{11}$$

where $F_D(\lambda)$ is the fluorescence intensity of the donor (with the area of the spectrum normalized to 1) and $\varepsilon_A(\lambda)$ is the molar absorption coefficient of the acceptor at wavelength λ (nm).

Using eq. 10, we obtained $R_0 = 6.8$ nm for dynamic, randomly oriented dipoles in buffer solution [19]. To model the FRET occurring between dT_{25}-ROX and dT_{25}-MG adsorbed onto the thermo-responsive polymer nanoparticles at different temperatures, we use a model that accounts for the kinetics of FRET between molecules in systems with restricted geometry [7]. According to the distribution model for energy transfer in confined spherical systems [7,41] the decay of the fluorescence emission $I_D(t)$ of the donor in the presence of acceptors is

$$I_D(t) = \exp(-t/\tau_D) \times \int_{Vs} C_D(r_D)\varphi(t, r_D) r_D^2 dr_D \tag{12a}$$

$$\varphi(t, r_D) = \exp\left\{ -\frac{2\pi}{r_D} \int_{Re}^{\infty} \left[1 - \exp(-w(r)t)\right] \times \left[\int_{|r_D - r|}^{|r_D + r|} C_A(r_A) r_A \, dr_A \right] r \, dr \right\} \tag{12b}$$

where V_S is the volume containing all donors in the particle, and $C_D(r)$ and $C_A(r)$ are the radial distribution profiles of donors and acceptors, respectively. We model these distributions with the Helfand and Tagami expression [42], deduced for planar polymer interfaces in strongly segregated systems, modified for spherical symmetry [41,43],

$$C(r) = \begin{cases} \dfrac{1}{2V_0}\left\{1 - \tanh\left[2(r - R_p)/\delta\right]\right\} & , \quad r > R_c \\ 0 \quad , \quad r < R_c \end{cases} \tag{13}$$

The fluorescence experimental decay, $I_D(t)$, can be determined only up to a constant factor so the donor concentration profile is given by $C_D(r) = C(r)$. The acceptor concentration profile $C_A(r)$ has units of number density and is given by $C_A(r) = n_A\, C(r)$, where n_A is the total number of acceptor molecules adsorbed on each particle. The encounter radius, R_e, is the minimum distance between donor and acceptor (usually set equal to the sum of the donor and acceptor van der Waals radii). The donor fluorescence decay curves of nanoparticle dispersions containing different ratios of adsorbed dT_{25}-ROX and dT_{25}-MG (Fig. 11) were fitted with eqs. 12–13, to obtain the distribution of adsorbed ODN in the particle shell for temperatures below and above T_{VPT} [19]. There are only three fitting parameters in the model: the average distribution radius R_p, the shell–water interface thickness δ, and a normalization factor for the intensity of the decay curve. The number of acceptor molecules in the shell was independently calculated from the mass balance of adsorbed dT_{25}-ROX. The critical Förster distance was kept fixed to the experimental value $R_0 = 6.8$ nm, the encounter radius was set at $R_e = 0.5$ nm [41]. The donor lifetime was also independently obtained from a dispersion containing only dT_{25}-ROX adsorbed to the particles, for which the fluorescence decay curves obtained at 23 and 45 °C could be fitted to a single exponential function with lifetimes $\tau_D = 4.8$ ns and $\tau_D = 4.6$ ns, respectively.

From the fit of the dT_{25}-ROX fluorescence decays in the presence of various amounts of dT_{25}-MG, we obtain the distribution of ODN adsorbed on the PNIPAM shell for each acceptor concentration (Fig. 12).

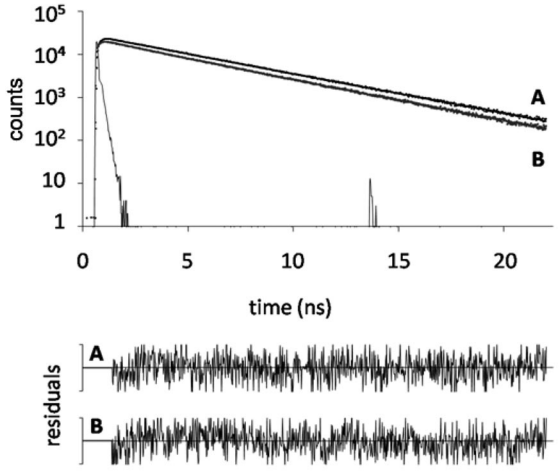

Fig. 11 Time-resolved fluorescence decay curves (λ_{exc} = 575 nm, λ_{em} = 615 nm) of dT_{25}-ROX (3.6 nmol/l) adsorbed in a 0.015 wt % dispersion of polymer nanoparticles (1 mM phosphate buffer solution with 1 mM NaCl and pH = 4.0) at 23 °C, with 5.4 nmol/l (A) and 45.3 nmol/l (B) of dT_{25}-MG. The weighted residuals correspond to fitting the experimental decays with eqs. 12–13.

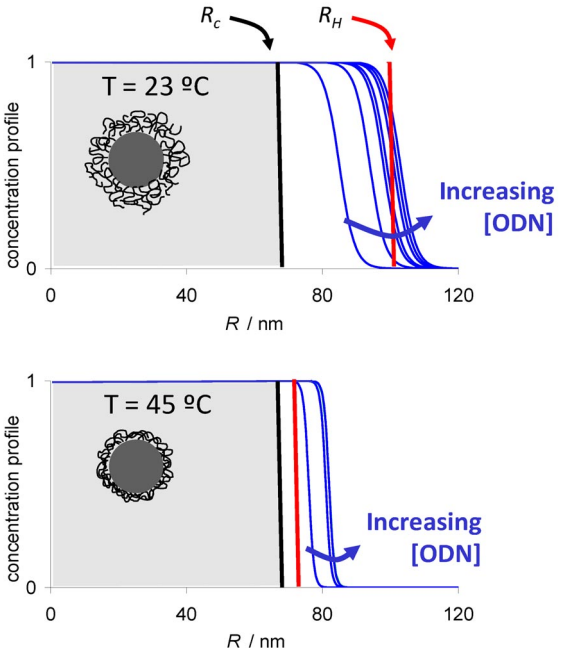

Fig. 12 Distribution profiles of ODNs adsorbed onto the core-shell particles (5.0×10^{-3} wt %) at 23 and 45 °C, calculated by fitting the donor fluorescence decay curves with eqs. 12a and 12b using the density functions of eq. 13 (shown normalized to 1). As the amount of adsorbed ODNs increases, the distribution of ODNs becomes broader (*blue curves*). Also shown, is the hydrodynamic radii of the core R_c (*dark line* defining the gray region) and the hydrodynamic radii of the particles R_H (*red line*).

The main characteristic of Fig. 12 is that the ODNs are distributed over a larger volume for temperatures below $T_{VPT} \approx 30$ °C. This was expected from the particle hydrodynamic radius determined by DLS. The fact that the recovered distributions are quite broad means that some of the ODN molecules should have the dye-labeled end closer to the core and others have it closer to the water phase. We also observe that the ODN distribution changes when the amount of adsorbed ODN is changed. With the increase in adsorbed ODNs, their distribution becomes broader, with the effect being more pronounced at 23 °C, when the PNIPAM shell is expanded.

At 23 °C, although the PNIPAM shell is swelled with water to an average length $L \approx R_p - R_c =$ 33 nm (the water content at this temperature is estimated to be above 90 %) [17], the ODN molecules are preferentially adsorbed near the PMMA core, gradually occupying the remainder of the shell as the ODN content is increased. For the higher amounts of ODN adsorbed, the breadth of the distribution obtained by FRET coincides with the hydrodynamic radius of the particles obtained by DLS, assuring us that the two techniques yield equivalent results. The size of the particles is not affected by the adsorption of ODN molecules in the concentrations used here (cf. Fig. 1), probably because the number of negative charges coming from the ODNs (25 per molecule, resulting in a maximum of ca. 10^4 per particle) is small compared to the amount of positive charges resulting from the charged comonomer plus the initiator residues in each particle (ca. 10^5 per particle).

When the temperature is increased to 45 °C, the PNIPAM shell collapses to about 10 % of its volume at 23 °C. Although the shell is only ca. 5 nm thick, it is able to keep all the adsorbed ODN, with no ODN release to the water phase being observed.

However, the most unexpected feature of the results is that at 45 °C the ODN distribution stretches out of the particle hydrodynamic radius especially for more than 100 ODNs per particle. This had not been detected by DLS probably because the low amount of ODN molecules per particle is not enough to change the hydrodynamic radius of the particle. This means that the ODN molecules remain adsorbed to the collapsed PNIPAM shell at one end, while the rest of the molecule extends into the water. The length of the ODN strand is estimated as ca. 8 nm (both by MD simulations and from the statistical monomer length) [19]. By comparing this value with the distribution length of ca. (14.7 ± 0.8) nm obtained at 45 °C for more than 100 ODN/particle, and the corresponding average shell thickness $L_{shell} \approx 5$ nm, we conclude that the ODN molecules should be relatively aligned perpendicularly to the particle surface, stretching into the water phase.

The amount of ODNs that are in the water phase can be estimated from the integral of the ODN distribution that lies outside the particle hydrodynamic volume determined by DLS. While at 23 °C, the adsorbed ODN are located inside the PNIPAM shell; at 45 °C, the volume fraction of ODN outside the particle shell is about 60 %, for more than 100 ODN/particle (Fig. 13). This is in agreement with the result obtained by comparing the refractive index of the particles shell with the refractive index of water and the dry PNIPAM (cf. eq. 2), which yielded a fraction of 60 % of the ODNs with the ROX in the water phase.

The results obtained by FRET correlate well with data obtained by fluorescence anisotropy for dT_{25}-ROX adsorbed into identical core-shell particles. The percentage of *immobile* ODNs increases with temperature, because they are entrapped in the shell which becomes more compact above T_{VPT}. On the other hand, the shorter rotational correlation time, θ_w, related to the rotation of the ROX at the tip of the ODN, and the larger rotational correlation time, θ_{oligo}, related to the rotation of the ODN as a whole, are compatible with the distribution of the dyes in the shell determined by FRET. Below T_{VPT}, the adsorbed ODNs show relaxation times identical to the ones obtained for the free ODN in water, confirming the very open structure of the PNIPAM shell with high water content. Above T_{VPT}, the anchoring of the adsorbed ODN to the collapsed particle shell results in smaller θ_{oligo}, than in water. On the other hand, the smaller rotation correlation time θ_w, corresponding to the faster dynamics of the dye at the tip of the dT_{25}-ROX, does not show any transition at T_{VPT}, because it corresponds to a local motion of the ODNs with the ROX end pointing toward the water and those in the shell are only slightly undisturbed by the PNIPAM chains. A closer observation of Fig. 12 also shows that the shape of the

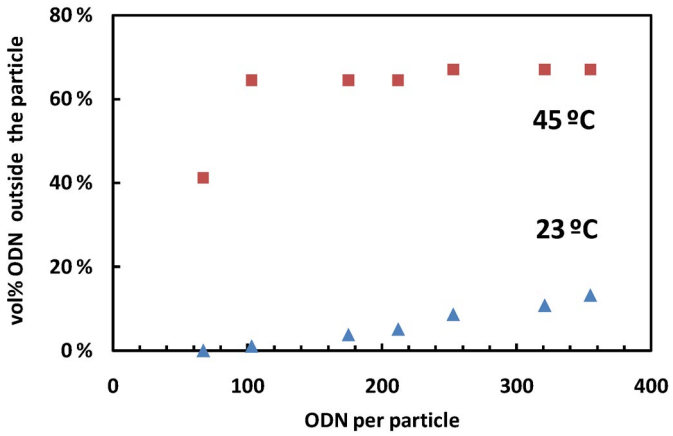

Fig. 13 The volume of the ODN distribution at 45 °C (■) and at 23 °C (▲), outside the particle volume determined by DLS. At 23 °C, almost all the adsorbed ODNs are located inside the PNIPAM shell, while at 45 °C the shell is collapsed and the ODNs extend into the water phase. The volume fraction of ODNs outside the particle shell at 45 °C is about 60 %, for more than 100 ODN/particle.

ODN distribution appears to be similar when the PNIPAM shell is extended (at 23 °C) and when it is collapsed with the ODN molecules protruding into the water phase (at 45 °C). In fact, the values of the δ parameter change from $\delta \sim 11$ nm to $\delta \sim 10$ nm when the temperature is increased from 23 to 45 °C. In spite of the difference in the conformation of the PNIPAM chains, the ODN molecules are mostly in an aqueous environment in both cases: while below T_{VPT}, the ODNs are adsorbed in the extended and hydrated PNIPAM shell; above T_{VPT}, the ODN molecules are anchored to a thin and less-polar collapsed shell of PNIPAM, but mostly extending into the water phase.

Bioassays

Figure 14 shows the fluorescence spectra of the Cgene-ROX (25 nM) adsorbed onto the core-shell particles (0.015 wt %) in the absence and presence of Gene-MG (35 nM) at high ionic strength (0.18 M NaCl) and pH = 4.0 (1 mM phosphate buffer and 1 mM EDTA). By adding the complementary gene, the fluorescence intensity decreases by about 70 %. This is due to the hybridization of the complementary ODNs that bring the MG close to the ROX, increasing the energy transfer efficiency. The efficiency of resonance energy transfer obtained in particles (70 %) is close to that obtained for the ODNs in solution. The possibility of a false assay due to the adsorption of the complementary ODN at the particle surface was checked using a dispersion of the polymer nanoparticles containing the same amount of Cgene-ROX and dT_{25}-MG (non-complementary ODN) in the place of Gene-MG. The fluorescence spectrum obtained is identical to that of the dispersion containing only Cgene-ROX (Fig. 14), thus excluding the possibility of a false positive result.

These preliminary results show that the thermoresponsive polymer nanoparticles can be used as a support in DNA assays. By using the particles, we can achieve the same hybridization efficiency as for the ODNs in solution at high ionic strength, while taking advantage of their high surface area, ease of chemical modification, separation, and possible reutilization.

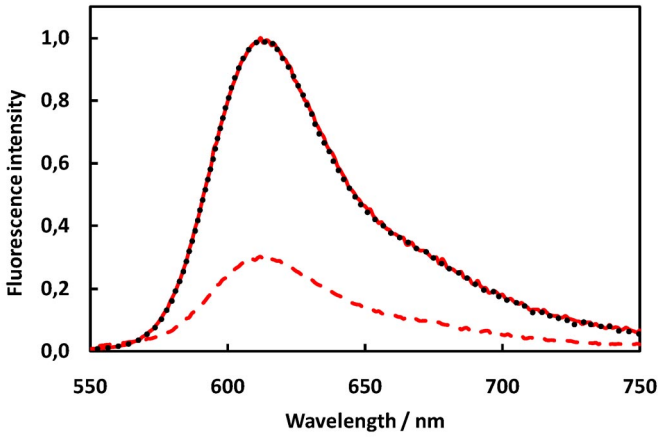

Fig. 14 Fluorescence spectra of Cgene-ROX (25 nM) adsorbed onto the polymer nanoparticles (0.015 wt %, 0.18 M NaCl, pH = 4.0, 1 mM phosphate buffer, and 1 mM EDTA) at 40 °C, before (*solid line*) and after (*dashed line*) adding Gene-MG (35 nM). If a noncomplementary ODN (dT_{25}-MG) is used in place of Gene-MG, no decrease in fluorescence emission is observed (*dotted line*).

CONCLUSIONS

The shell of thermoresponsive core-shell polymer nanoparticles was characterized using an ODN labeled with a rhodamine dye (dT_{25}-ROX). The polarity of the PNIPAM shell determined from both the lifetimes and the solvatochromic shifts shows an abrupt change with temperature at the T_{VPT}. FRET between dT_{25}-ROX and dT_{25}-MG can be used to calculate the distribution of the ODNs in the thermoresponsive shell.

At 23 °C, below the T_{VPT}, FRET shows that the ODNs are distributed in the interior of the shell, and the polarity indicates that ROX senses an environment similar to water (the shell is composed of highly hydrated PNIPAM chains). Fluorescence anisotropy measurements show that below T_{VPT}, the ODNs are highly mobile.

By increasing the temperature above T_{VPT}, the shell thickness decreases from 42 to 5 nm and the mobility drastically slows down. The FRET results show that the ODN are not located inside the thin particle shell (~5 nm). The polarity probed by the ROX averages the dye distribution between the interior and exterior of the particle shell. The percentage of dye outside the particle shell that sense pure water determined from the lifetimes (refractive index) is ca. 60 %, in agreement with the volume fraction calculated from the FRET distribution functions (cf. Fig. 13). The drastic mobility loss of the ODNs at temperatures above T_{VPT} results from their anchor in the dense collapsed particle shell. The identical rotation relaxation times of the ROX moiety at the ODN chain-end in water and when adsorbed onto the particles reflect the fact that most of the adsorbed ODNs are oriented with the dye toward the water phase.

These results lead us to use the thermoresponsive particle as supports for ODNs in hybridization assays. The hybridization efficiency obtained from FRET with the supported ODNs is identical to the value found in solution, a very promising result regarding the use of the particles as supports in bioassays.

ACKNOWLEDGMENTS

The authors thank FCT for financial support under project: PDCT/CTM/68451/2006. T.J.V.P thanks FCT for a post-doc grant (SFRH/BPD/27175/2006).

REFERENCES

1. B. Valeur. *Molecular Fluorescence: Principles and Applications*, Wiley-VCH, New York (2001).
2. J. Lacowitz. *Principles of Fluorescence Spectroscopy*, 2nd ed., Kluwer Academic, Dordrecht (1999).
3. I. Z. Steinber, E. Hass, E. Katchalsi. "Long-range nonradiative transfer of electronic excitation energy", in *Time-Resolved Spectroscopy in Biochemistry and Biology*, S. St. Andrews (Ed.), Plenum, New York (1983).
4. P. S. Eis, J. R. Lakowicz. *Biochemistry* **32**, 7981 (1993).
5. B. P. Maliwal, J. R. Lakowicz, G. Kupryszewski, P. Rekowski. *Biochemistry* **32**, 12337 (1993).
6. K. M. Parkhurst, L. J. Parkhurst. *Biochemistry* **34**, 293 (1995).
7. J. P. S. Farinha, J. M. G. Martinho. *J. Phys. Chem. C* **112**, 10591 (2008).
8. J. M. G. Martinho, K. Sienicki, D. Blue, M. A. Winnik. *J. Am. Chem. Soc*. **110**, 7773 (1988).
9. J. M. G. Martinho, M. A. Winnik. *Macromolecules* **19**, 2281 (1986).
10. S. Nayak, L. A. Lyon. *Angew. Chem., Int. Ed.* **44**, 7686 (2005).
11. C. Pichot. *Curr. Opin. Colloids Interface Sci.* **9**, 2132 (2004).
12. K. Kawaguchi. *Prog. Polym. Sci.* **25**, 1171 (2000).
13. A. Elaïssari. *Prog. Colloid Polym. Sci.* **133**, 9 (2006).
14. A. Kumar, A. Srivastava, I. Y. Galaev, B. Mattiasson. *Prog. Polym. Sci.* **32**, 534 (2007).
15. Z. M. O. Rzaev, S. Dinçer, E. Piskin. *Prog. Polym. Sci.* **32**, 1205 (2007).
16. A. M. Santos, A. Elaïssari, J. M. G. Martinho, C. Pichot. *Polymer* **46**, 1181 (2005).
17. T. J. V. Prazeres, A. M. Santos, J. M. G. Martinho, A. Elaïssari, C. Pichot. *Langmuir* **20**, 6834 (2004).
18. T. J. V. Prazeres, A. Fedorov, J. M. G. Martinho. *J. Phys. Chem. B* **108**, 9032 (2004).
19. T. J. V. Prazeres, J. P. S. Farinha, J. M. G. Martinho. *J. Phys. Chem. C* **112**, 16331 (2008).
20. A. A. Dar, G. M. Rather, A. R. Das. *J. Phys. Chem. B* **111**, 3122 (2007).
21. J. P. S. Farinha, J. G. Spiro, M. A. Winnik. *J. Phys. Chem. B* **105**, 4879 (2001).
22. J. P. S. Farinha, J. M. G. Martinho, L. Pogliani. *J. Math. Chem.* **21**, 131 (1997).
23. E. S. Gil, S. A. Hudson. *Prog. Polym. Sci.* **29**, 1173 (2004).
24. F. M. Winnik. *Macromolecules* **23**, 1647 (1990).
25. H. G. Schild, D. A. Tirrell. *J. Phys. Chem.* **94**, 4352 (1990).
26. S. Fujishige, K. Kubota, I. Ando. *J. Phys. Chem.* **93**, 3311 (1989).
27. X. Wang, X. Qui, C. Wu. *Macromolecules* **31**, 2972 (1998).
28. T. Karstens, K. Kobs. *J. Phys. Chem.* **84**, 1871 (1980).
29. J. Karpiuk, Z. R. Grabowski, F. C. DeSchryver. *J. Phys. Chem.* **98**, 3247 (1994).
30. D. Magde, G. E. Rojas, P. G. Seybold. *Photochem. Photobiol.* **70**, 737 (1999).
31. S. J. Strickler, R. A. Berg. *J. Chem. Phys.* **37**, 814 (1962).
32. *Handbook of Chemistry and Physics*, 78th ed., CRC Press, New York (1997).
33. J. Gao, C. Wu. *Macromolecules* **30**, 6873 (1997).
34. M. J. Harley, D. Toptygin, T. Troxler, J. F. Schildbach. *Biochemistry* **41**, 6460 (2002).
35. K. Kinosita, S. Kawato, A. Ikegami. *Biophys. J.* **20**, 289 (1977).
36. G. Lipari, A. Szabo. *Biophys. J.* **30**, 489 (1980).
37. G. B. Dutt. *J. Phys. Chem. B* **106**, 7398 (2002).
38. T. J. V. Prazeres, A. Fedorov, S. P. Barbosa, J. M. G. Martinho, M. N. Berberan-Santos. *J. Phys. Chem. A* **112**, 5034 (2008).
39. T. Förster. *Ann. Phys. (Leipzig)* **2**, 55 (1948).
40. T. Förster. *Z. Naturforsch., A: Phys. Sci.* **4**, 321 (1949).
41. (a) J. P. S. Farinha, K. Schillen, M. A. Winnik. *J. Phys. Chem. B* **103**, 2487 (1999); (b) J. P. S. Farinha, J. M. G. Martinho, S. Kawaguchi, A. Yekta, M. A. Winnik. *J. Phys. Chem.* **100**, 12552 (1996).

42. E. Helfand, Y. Tagami. *J. Chem. Phys.* **56**, 3592 (1972).
43. J. P. S. Farinha, M. T. Charreyre, J. M. G. Martinho, M. A. Winnik, C. Pichot. *Langmuir* **17**, 2617 (2001).